Journal of Translational Medicine

RESEARCH

Open Access

A semi-automatic pipeline integrating histological and µCT data in a mouse model of lung fibrosis

Elena Vincenzi[1†], Martina Buccardi[2,3†], Erica Ferrini[3,4], Alice Fantazzini[1], Eugenia Polverini[2], Gino Villetti[3], Nicola Sverzellati[5], Andrea Aliverti[6], Curzio Basso[1], Francesca Pennati[6] and Franco Fabio Stellari[3*]

Abstract

Background Drug discovery strongly relies on the thorough evaluation of preclinical experimental studies. In the context of pulmonary fibrosis, micro-computed tomography (µCT) and histology are well-established and complementary tools for assessing, in animal models, disease progression and response to treatment. µCT offers dynamic, real-time insights into disease evolution and the effects of therapies, while histology provides a detailed microscopic examination of lung tissue. Here, we present a semi-automatic pipeline that integrates these readouts by matching individual µCT volume slices with the corresponding histological sections, effectively linking densitometric data with Ashcroft score measurements.

Methods The tool first geometrically aligns the vertical axis of the µCT volume with the cutting plane used to prepare the histological sample. Then, focusing on the left lung, it computes the affine registration that identifies the µCT coronal slice that best matches the histological section. Finally, quantitative µCT imaging parameters are extracted from the selected slice. In a proof-of-concept test, the tool was applied to a bleomycin-induced mouse model of lung fibrosis.

Results The proposed approach demonstrated high accuracy and time effectiveness in matching µCT and histological sections minimizing manual intervention, with an overall success rate of 95%, and reduced time required to align µCT and histological data from 40 to 5 min. Significant correlations were found between quantitative data derived from µCT and histology data.

Conclusions The precise combination of microscopic ex-vivo information with 3D in-vivo data enhances the accuracy and representativeness of tissue analysis and provides a structural context for omic studies, serving as the foundation for a multi-layer platform. By facilitating a detailed and objective view of disease progression and treatment response, this approach has the potential to accelerate the development of effective therapies for lung fibrosis.

Keywords Bleomycin model, Lung fibrosis, Deep learning, Drug discovery, Micro-computed tomography, Histology

†Elena Vincenzi and Martina Buccardi have contributed equally to this work.

*Correspondence:
Franco Fabio Stellari
fb.stellari@chiesi.com
Full list of author information is available at the end of the article

Background

Histological examination, routinely performed in clinical practice, is the gold standard for analyzing tissue changes and staging diseases [1]. Despite its indisputable usefulness and widespread utilization, this approach suffers from several limitations: it covers only a limited portion of the lungs, it does not allow for longitudinal sampling, and it requires biopsy procedures, which involve discomfort and risk for the patient [2]. Histological analysis is also a typical terminal procedure in preclinical studies where, for highly resolved 2D regions of the interested organs, it provides information at a cellular level, while precluding longitudinal examinations and the acquisition of three-dimensional features [3, 4]. Furthermore, tissue distortion may occur during paraffinization and mechanical cutting of the samples. Conversely, in-vivo μCT imaging has a more limited micron resolution but allows for non-destructive 3D visualization of the organ and delivers valuable information complementary to that provided by histology [5–8]. While μCT can capture macroscopic changes and track disease progression longitudinally, histology provides detailed endpoint assessments of tissue structure and cellular alterations [9–11]. The integration of these technologies represents a significant advancement in various animal models, including preclinical pulmonary research, as combining in-vivo and ex-vivo assessments allows for a more comprehensive staging of the disease and evaluation of putative drugs with the possibility of monitoring disease progression through serial imaging, followed by endpoint determination of parenchymal changes via histological analysis [9–11]. The matching of μCT and histology has the potential to be applied in other biomedical areas as well. Specifically, μCT can (i) help guide histological sampling by identifying specific areas of interest, ensuring that diverse regions of the lung are adequately represented, and (ii) data from proteomic and transcriptomic analyses derived from histological samples could be correlated with the 3D structure of the lung, providing spatial context, and associated with in vivo structural and functional information. A well-matched combination of these approaches can provide integrated functional and molecular biomarkers that may lead to a more detailed, and more reliable monitoring of both disease progression and the effectiveness of novel therapeutic interventions.

However, image registration between 2D histological sections and 3D μCT scans is challenging. A major issue is associated with the sectioning of paraffin-embedded soft tissues, which can introduce non-uniform deformations, especially in porous tissues such as the lung [12]. The primary challenge is determining the exact position of the cutting plane in a three-dimensional space. This is particularly relevant because any tissue alteration or damage on the histological slide may lead to shifts in the tissue-slicing process, thereby hindering the subsequent two-dimensional-to-two-dimensional problem (i.e. matching between 2D μCT slice to 2D histological slide). Therefore, the overall procedure can be divided into two main steps: first, identifying the cutting plane in the 3D μCT volume and then matching it with the 2D histological slice. Various strategies, ranging from manual identification of the cutting plane [12] to semi-automatic and automatic approaches, have been proposed to address this problem. Two-stage approaches, with an approximate preliminary positioning and a subsequent fine alignment have been proposed in clinical settings, especially for bone tissue [13–15]. In this case, the plane in the 3D volume is initially aligned by bringing it close to a group of candidate sections. This is followed by a refined correction of plane displacements and tilts based on the alignment of superimposable extrinsic markers and matched pixel/voxel intensities. Landmark-based approaches have also been proposed for clinical applications [16–18]. Regarding the preclinical setting, specifically, Museyko et al. [19] applied a semi-automatic registration method, relying on conventional intensity-based registration techniques, to mouse vertebrae and tibiae. To our knowledge, there have been no publications so far on the alignment of 2D histological slides to 3D μCT images of the lungs. Moreover, since soft tissue such as lung parenchyma is highly susceptible to deformation during paraffin embedding, the bronchial tree and the main pulmonary vessels are the only reliable landmarks that can be used for guiding the matching process.

In the present work, we describe a semi-automatic tool for matching 3D lung μCT scans with 2D histological images. Following an initial geometric alignment to overlay the vertical axis of the μCT volume with the cutting plane used for histological preparation, the process involves the extraction of a 2D coronal μCT slice that (best) matches the histological image. Our goal was to develop a semi-automatic method enabling the merging of pulmonary histological and μCT data. In a proof-of-concept validation, the method has been applied to a mouse model of bleomycin-induced lung fibrosis. The proposed pipeline allowed the extraction of quantitative μCT imaging biomarkers from the selected 2D slice to be used for comparison with ex-vivo data, thus underlining the usefulness of the proposed solution as a novel tool capable of integrating multi-modal imaging parameters, while reducing manual interventions.

Materials and methods

Animal model

All experiments were carried out on 8–10-weeks-old male C57Bl/6 mice purchased from Envigo (San Pietro

al Natisone, Udine, Italy). The animals were housed in groups of five per cage under standard conditions, following the guidelines outlined in the European Directive 2010/63/UE, Italian D.Lgs 26/2014, and the revised "Guide for the Care and Use of Laboratory Animals" (National Research Council Committee, US, 2011) [20]. The study was conducted in an AAALAC (Association for Assessment and Accreditation for Laboratory Animal Care) certified facility at Chiesi Farmaceutici and was approved by the Italian Ministry of Health (protocol number n° 809/2020-PR) and by the internal AWB (Animal Welfare Body). Upon delivery, the animals were acclimatized to our local vivarium conditions for 7–10 days (room temperature: 20–24 °C; relative humidity: 40–70%; 12 h light–dark cycle; food and water ad libitum). All necessary measures were taken to minimize pain or discomfort to the animals. A designated veterinarian or trained technician evaluated pain levels daily using a Visual Analogue Scale (VAS) ranging from 0 to 10. Humane endpoints were defined as the presence of dyspnea, body weight loss ≥ 20%, and VAS ≥ 6.

In the BLM group, pulmonary fibrosis was induced by administering bleomycin hydrochloride (Baxter) diluted in 50 µl saline via a triple (day 0, 2, 4) oropharyngeal aspiration (OA) under 2.5% isoflurane anesthesia, following previously described methods [8, 21, 22]. The negative control group received a triple OA of saline (SAL).

µCT protocols

Acquisition: mice were anesthetized with 2% isoflurane and scanned on a Quantum GX µCT (PerkinElmer, Inc. Waltham, MA). Lungs were scanned with X-ray tube voltage of 90 kV, and current of 88 µA, using the 'high speed' acquisition mode which is the fastest acquisition modality supported by the Quantum GX which also allows for gating monitoring. Briefly, after placing the animal on the scanner bed in supine position, the chest is aligned within the field of view using X, Y, and Z axis motorized stage controls in live mode with the respiratory region of interest (ROI) positioned over the diaphragm. The gating signal, the respiratory cycle lengths and the respiratory rate were monitored by reading the values inside the Respiratory Synchronization window. Projection images were collected in list-mode over a single continuous gantry rotation of 360°, total rotation time of 4 min, and 14,688 raw projections acquired, one per 16.33 ms (one per 0.024° angle of rotation). End-inspiratory (P01) and end-expiratory (P02) projections were retrospectively sorted (on average 900 projections for each phase) and automatically reconstructed using a GPU-based filtered back-projection algorithm with a Ram-Lak filter. Reconstructions were performed in axial slice orientation with the array size of 512 × 512 × 512 and with 50-µm isotropic voxels size. The system is calibrated monthly with standard phantoms for noise, uniformity, low contrast, and resolution [23].

Conversion from grey levels to Hounsfield Unit (HU): it was performed with a homemade phantom containing water and air. The phantom was acquired both at the beginning and at the end of each imaging session to ensure system stability in "High Speed" mode without the gating with the following parameters: X-ray tube voltage, 90 kV; CT X-ray tube current, 88 µA; acquisition time: 8 s. Greyscale to HU conversion was then achieved by computing the intercept and slope values derived from the equation of the line passing through the points (− 1000 HU, mean of air grey level) and (0 HU, mean of water grey level), where the mean air and water grey levels were obtained by averaging the air and water grey levels of the two phantom images.

Segmentation of the lungs: A deep convolutional neural network (CNN) with U-Net architecture, previously introduced for automatizing µCT-based densitometry on murine models of lung fibrosis, was employed to automatically segment, left and right lungs, and pulmonary airways [6, 21, 24]. Briefly, the segmentation module uses a multi-resolution strategy with two CNN models: a low-resolution model for initial processing, and a high-resolution 2.5D CNN model for segmenting the image in different planes, and then consolidating the segmentation outcomes through voting. The algorithm achieved a Dice score of about 0.97 in rigorous evaluations [6, 24].

Lung histology

On day 21, animals were sacrificed due to an anesthetic overdose followed by abdominal aortic hemorrhage. For histological investigation, the lungs were excised and inflated through the trachea with 0.6 ml of 10% neutral-buffered formalin and kept for 24 h. For each sample, a slice (5 µm) including the pulmonary hilum is cut with a rotary microtome (Slee Cut 6062, Slee Medical, Mainz, Germany) in the dorsal plane (coronal section). The sections were stained with Masson's Trichrome to assess fibrotic changes, according to the manufacturer's specifications (Histo-Line Laboratories). Histological slides were acquired as whole slide images (WSI) by the Nanozoomer S-60 digital slide scanner (Hamamatsu, Japan).

Multiple 10X magnification fields were examined for each sample, and experienced histopathologists blindly graded the morphological changes using the Ashcroft score (AS) scale [3, 25]. Lung parenchyma was classified based on fibrosis severity into three classes: no/mild (AS ≤ 3), moderate (AS = 4), and severe (AS ≥ 5) [9, 25]. The average AS score on the left lung (AS_L) was then calculated for each animal, while the Ashcroft frequency

distribution was expressed as the percentage of each fibrosis severity class (%Mild, %Moderate, %Severe).

Processing pipeline

The proposed pipeline aims to find the µCT coronal slice that closely resembles the section obtained from histology, and then perform densitometric analysis on the identified image.

Following µCT and histology image acquisition (Fig. 1a, b), the matching algorithm takes as inputs the segmented µCT volume and the histological slice corresponding to the sixth level of magnification of the microscope (Fig. 1c). Then, four main steps (Fig. 1d) constitute the core of the processing pipeline: (1) automatic µCT scans re-orientation; (2) user-guided identification of the regions to be matched in CT and histology and automatic setting of the constraints to the research space; (3) automatic slice selection; (4) output: best match and 2D-densitometry analysis.

Re-orientation of the CT volume is required to aligned µCT coronal slices with the histological image. In fact, before any manipulation, the virtual coronal cutting plane applied to the µCT volume differs from the cutting plane used in histology (Fig. 1a, b, green line). This is because the orientation of in-vivo imaged lungs varies depending on the animal anatomy and the mouse's position in the scanner. As a result, the coronal plane's position also varies. On the other hand, histological sample inclusion in paraffin is more standardized with the coronal cutting plane's orientation usually fixed and parallel to the ground.

The second step of the processing pipeline involves the accurate delineation of the regions of interest (ROI) that will be matched which, in both re-oriented CT and histological images, consist of the left lung lobe and the left branches of the airways included in the lung. Airways are included in the ROI since they serve as critical landmarks for alignment (Fig. 1d).

The right lung was not considered in the ROI since there is no correspondence between the right lung in CT and histology. This is because of the right lung anatomy consisting of four lobes which change and random spatial distributed during the paraffin inclusion procedure, since they are likely to separate, potentially impacting the efficacy of the registration algorithm.

In addition, to reduce computational requirements and improve registration accuracy, we limited the range of coronal slices eligible for matching, by defining realistic physical boundaries, through prior knowledge about the acquisition of histological sections and inquiring the user whether the primary airway branch is visible in the histological image (Supplementary Fig. 1).

At this point, co-registration between the histological slice and each coronal slice of the µCT in the acceptability range is performed, and the coronal slice achieving the highest metric is selected. On the selected slice, densitometric parameters are computed to be compared with histological derived parameters.

Re-orientation of the µCT volume

To achieve optimal µCT volume rotation, the left and right lungs should be aligned horizontally, and the volume adjusted to make the mouse's spine vertical (Fig. 2). This results in a rotation of the µCT volume around the z-axis to align the right and the left lung with the horizontal plane, followed by a rotation around the x-axis to align the spine parallel to the z-axis. Angle extraction and the subsequent rotation are completely automated.

The z-axis rotation angle α is measured on the axial plane by using the lowest y-coordinate point from the right and left lungs, which are extracted from the central section of the lung volume. The α angle is defined as the angle formed between the line connecting these points and the horizontal axis (Fig. 2b, pink).

The x-axis rotation angle β is determined on the sagittal plane by identifying coronal slices with a visible spine. A thresholding process segments the skeleton, including the spine and other bones, with voxel values above + 500 HU considered part of the skeleton. The rotation angle β is calculated as the median of the angles between the line passing through the highest and lowest lung points (Fig. 2b, green) projected onto the spine and the vertical axis for each section (Fig. 2b, blue). The lung mask resulting from the DL-segmentation step is automatically rotated with the µCT volume.

(See figure on next page.)

Fig. 1 Proposed pipeline. **a** µCT image acquisition; **b** histology image acquisition; **c** the inputs to the matching algorithm are the segmented µCT volume and the histology slice corresponding to the sixth magnification level of the microscope. **d** The processing pipeline consists of four main steps: (1) Reorientation of Micro-CT scans aimed at obtaining coronal µCT slices that are comparable with histological images because the virtual coronal cutting plane applied to the µCT volume differs from the cutting plane used in histology (green line). (2) In both CT and histology reoriented images, the region of interest (ROI) must be accurately delineated. In addition, the delimitation of the coronal slice search space was constrained using knowledge of the histologic acquisition. (3) Co-registration between the histological slice and each coronal slice of the µCT in the acceptability range is performed, and the coronal slice that obtains the highest metric is selected. (4) Ouput: Densitometric parameters are calculated on the selected slice to be compared with histology-derived parameters

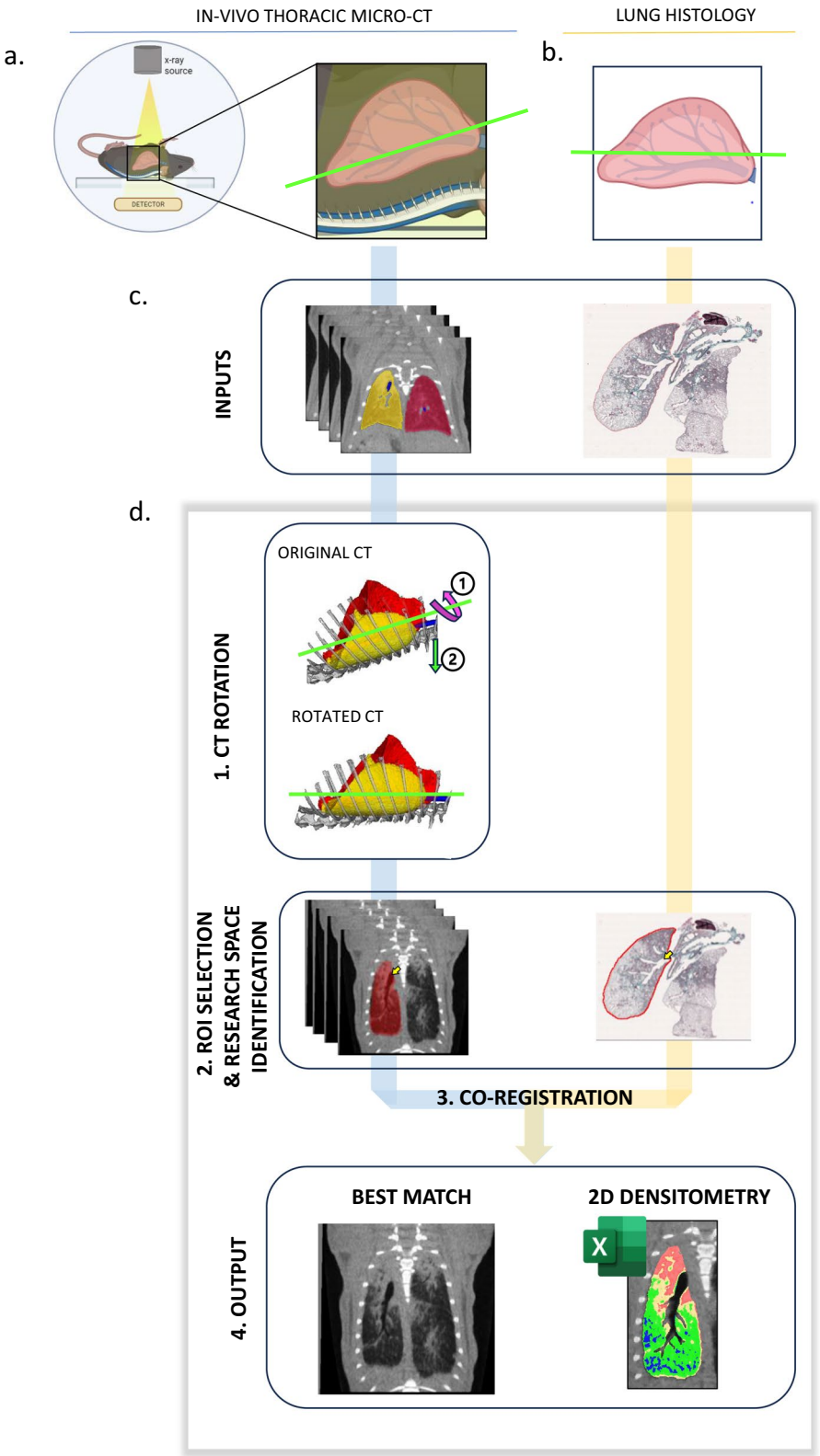

Fig. 1 (See legend on previous page.)

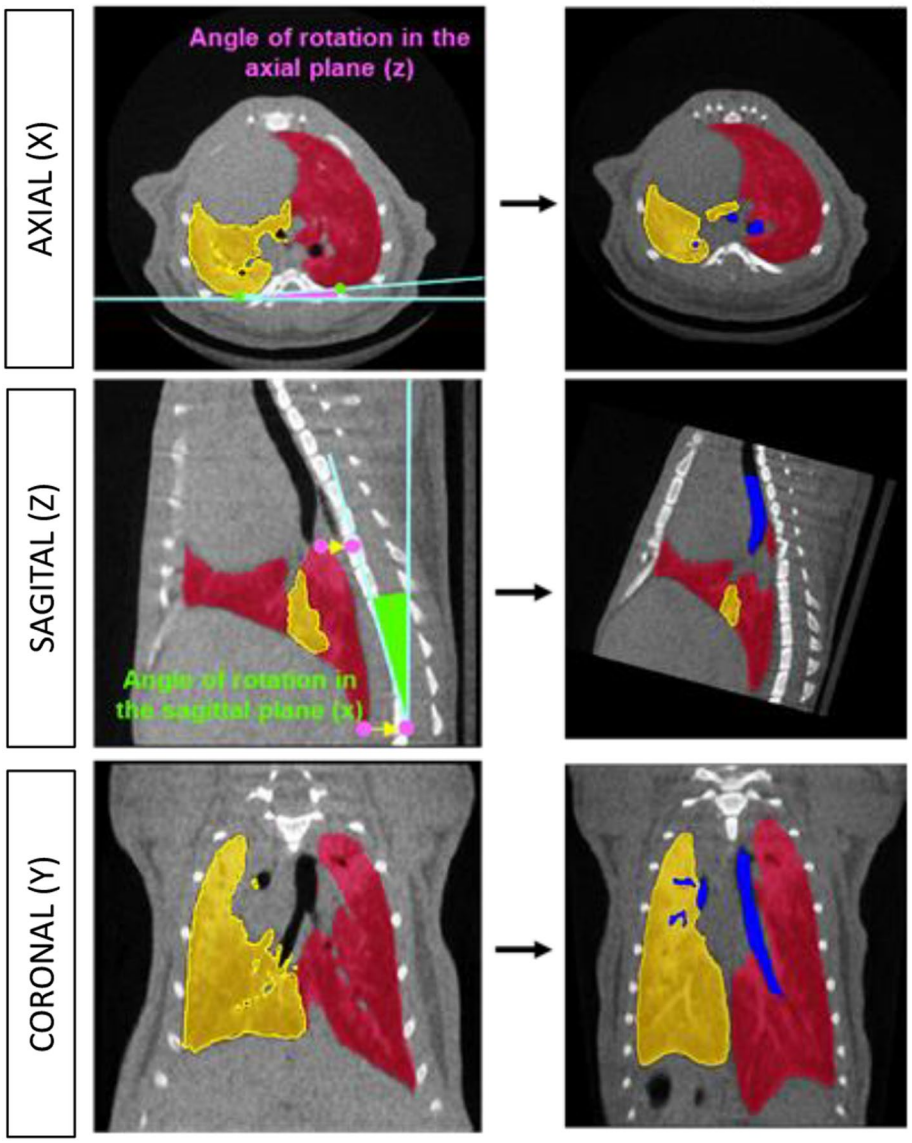

Fig. 2 Re-orientation of the micro-CT volume. To achieve optimal μCT volume rotation of the lungs of a mouse, one must horizontally align the left and right lungs and make the spine vertical. First, you rotate the volume around the z axis to align the lungs. The angle of rotation, α, is measured in the axial plane between the line connecting the lowest points of the lungs and the horizontal axis. Then, you rotate around the x-axis to align the spine parallel to the z-axis. The angle of rotation, β, is determined in the sagittal plane by segmenting the skeleton and calculating the median of the angles between the extreme points of the lungs projected onto the spine and the vertical axis

Extraction of the ROIs and constraints of the physical space

ROI segmentation. Since the best match is sought by considering only the left lung and the airway branches contained in it, it is necessary to identify the ROIs that will be matched on the re-oriented μCT scan and histological image.

On re-oriented μCT, the re-oriented lung mask is refined by creating a convex hull. The convex hull effectively encompasses all lung points and helps avoid overfilling in comparison to densely filling unsegmented areas. The airway portion within the convex hull of the left lung is selected using a multiplication operation. The resultant segmentation, which includes the left lung and its enclosed airways, is considered as the μCT ROI in the proposed pipeline (Fig. 3a).

On histological picture, the left lung is segmented with a GrabCut algorithm [26]. A graphical user-friendly interface featuring two windows are provided for semi-automatically selecting the ROI in the histological image (Fig. 3b). The interface includes an

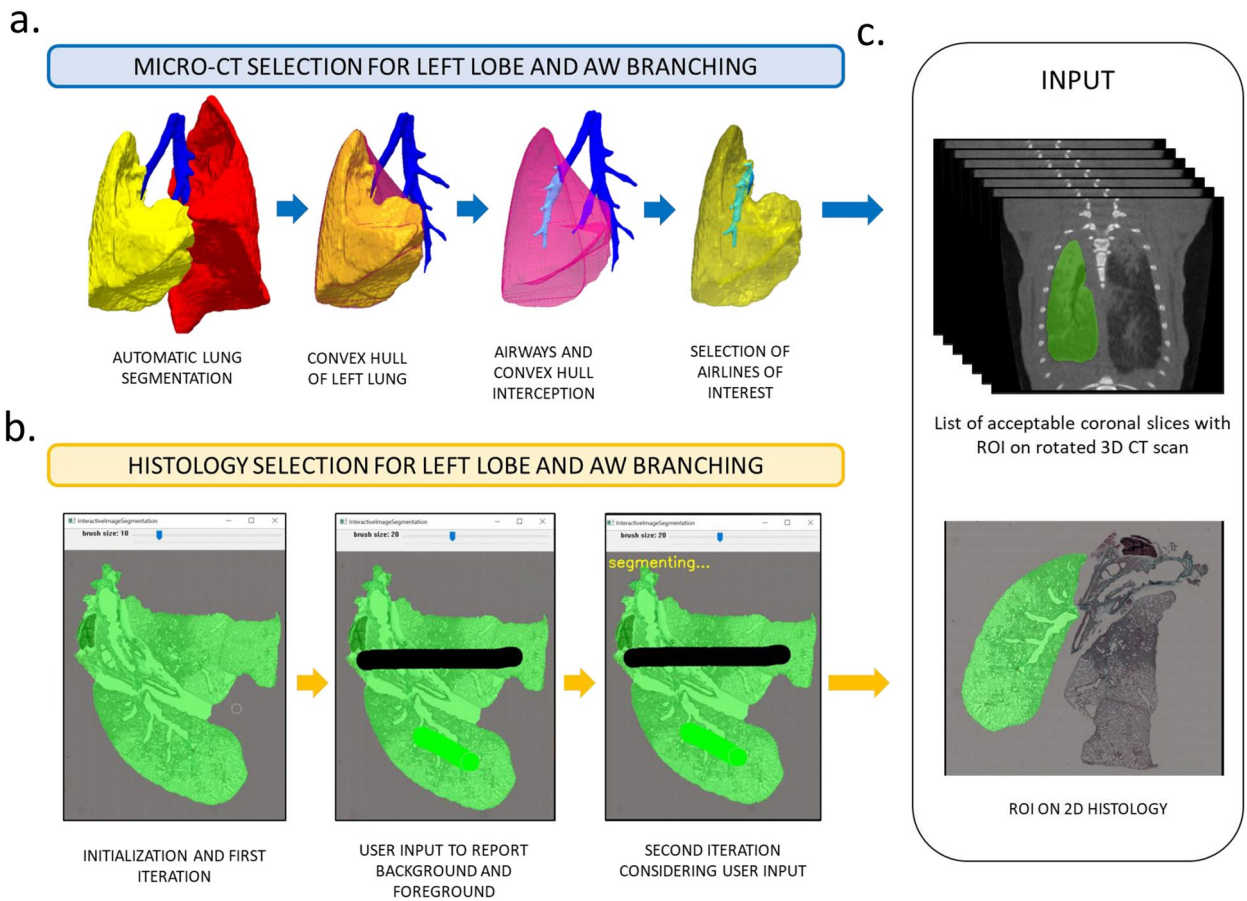

Fig. 3 Extraction of the ROIs and constraints of the physical space. **a** Left lung and left airway branches selection on Micro-CT. From left to right: an example of the 3D rendering generated by automatic segmentation. The left lung (in yellow) and airway (in blue) are then selected, and a convex hull is performed. The airways contained within the left lung (in cyan) are isolated by taking the intersection between the airways and the convex hull (magenta). This intersection constitutes the ROI on the rotated CT scan. **b** Left lung and left airway branches selection on Histology. The tool includes a semi-automatic interactive graphical user interface by which the user can select the ROI. From left to right: The user can mark areas belonging to the background (in black) or the ROI (in green) using a brush. The interface then proposes a new segmentation based on the input. The process can be iterated until only the left lung is contained in the ROI. **c** Input of the matching procedure. The matching procedure takes as input a list of acceptable 2D coronal slices from the micro-CT with the associated ROI and the histological image with its associated ROI

interactive panel showing the initial segmentation result based on the GrabCut algorithm (green = object pixels, black = background pixels), overlaid on the histological image with transparency, along with a separate window showing the resulting segmentation. This algorithm represents pixel colours in the image using a multivariate Gaussian mixture. Through iterations, the algorithm updates the segmentation by estimating Gaussian parameters based on pixel proximity and probabilistically assigning labels to each pixel. Convergence is reached when pixel labels remain stable between iterations. The user can further refine the segmentation by marking areas as background or foreground using the interface brush, allowing for multiple iterations until satisfactory results are obtained.

Constrain of the search space: The research space for finding the optimal μCT coronal slice matching the histological section was restricted to reduce the computational burden. Indeed, histological sectioning is performed in the first third of the lung, a strategic positioning for providing a comprehensive view across both hilar and peripheral lung regions, enhancing the detection of potential lesions. The first limit was set as the slice where the spine is no longer a continuous line, and the second as the slice where the lungs touch because of the accessory lobe (Supplementary Fig. 1). These limits were set together with experts and were chosen as

reasonable limits in which the histological cut may have been performed.

Furthermore, to narrow down the research range, users are asked whether the main left bronchi is visible in histology: if the branch is visible, the search is confined to sections with an airway area of at least 1.5 mm^2; otherwise, the search is restricted to sections lacking main airways (airway area less than 1.5 mm^2).

Co-registration of the µCT with the histological section

To set up image registration, the two images must be in the same physical space. The scale factor for resampling an image can be computed by dividing the histology spacing by the µCT spacing, as the pixel dimensions differ between histology (0.625 × magnification, pixel 0.028 mm) and µCT (voxel 0.05 mm). After resampling the histological image is co-registered with each of the 2D coronal slices within the research range established in the previous step. A multi-resolution ("coarse-to-fine") approach is employed using a Gaussian pyramid with 3 levels coupled with a stochastic optimization method. The similarity measure between the registered and the reference images is iteratively estimated from the coarsest (low resolution image) to the finest (highest resolution) level of the pyramid. This strategy not only reduces the computational cost of the co-registration, but also minimizes the risk of encountering local minima during the optimization procedure [27, 28]. To further reduce the computational costs, only a fraction of the voxels of the image (75% sampled with regular strategy) is used to estimate the measure of similarity.

The co-registration procedure consists of two-steps: first, a global affine transformation, initialized by aligning the centre of mass of the histology and µCT ROIs, is estimated to roughly align the images. Next, another affine transformation is estimated to more finely align the two images based on the normalized mutual information, since the number of points between the two images is different. In both phases, the interpolator is linear, and the optimizer is the gradient descent with a learning rate of 1. The maximum number of iterations is set to 100, and the convergence value to 10^{-8}.

Each coronal slice is associated with a metric evaluation value. The slice with the highest metric value is chosen as the solution to the problem, as illustrated in Fig. 4.

2D densitometry on µCT

From the selected 2D coronal slices, the tool automatically derived left lungs areas and MLA densities (measured in Hounsfield Units, HU) together with other biomarkers of interest and aeration compartments (Table 1). For the phantom-based grayscale to Hounsfield units conversion, the ranges for the aeration compartment were adapted from those computed by Mecozzi et al. [10].

In addition to the quantitative values, an image representing densitometry is also produced using the following colour codes: blue = hyper-aerated, green = normo-aerated, yellow = hypo-aerated, red = non-aerated (Fig. 1d).

Validation

The proposed pipeline was tested on an NVIDIA Tesla P40 graphics card with CUDA = 6.1 computational capability, under Windows operating system.

The accuracy of the process was determined by assessing: (1) the rotation angles, and (2) the selected coronal slices.

Rotation angles accuracy was determined on a sample of 22 mice divided in 9 SAL and 12 BLM. This was done by comparing the automatic and manual reorientation of the µCT volume. Manual re-orientation was performed using Analyze software (Analyze 14.0; Copyright 1986–2017, Biomedical Imaging Resource, Mayo Clinic, Rochester, MN). As for the previously described automatic procedure, manual re-orientation also involved first aligning the left and right lungs in the axial plane followed by positioning the mouse's spine vertically along the sagittal view.

The accuracy of the selected coronal slices was evaluated on a total of 60 mice (10 SAL and 50 BLM) by comparing the manually selected slice number after automatic re-orientation with the slice number chosen automatically by the proposed pipeline.

The automatically selected µCT coronal slice should comprise densitometric biomarkers closely resembling the tissue-specific features measured by histology [5, 6, 9, 10, 21]. Therefore, to confirm that the proposed process matches reasonable µCT slices with histological sections, µCT-derived densitometry and histological Ashcroft Score measured on the left lung (AS_L) were compared in samples in which a difference of up to 10 slices was observed between automatically and manually selected slices (57 of 60 mice).

Statistics

Statistical analyses were performed with the Prism 8 software (GraphPad Software Inc., San Diego, CA, USA). Correlation between µCT readouts and the Ashcroft scores was assessed by calculating Spearman correlation coefficients. The statistical significance threshold was set at a $p < 0.05$.

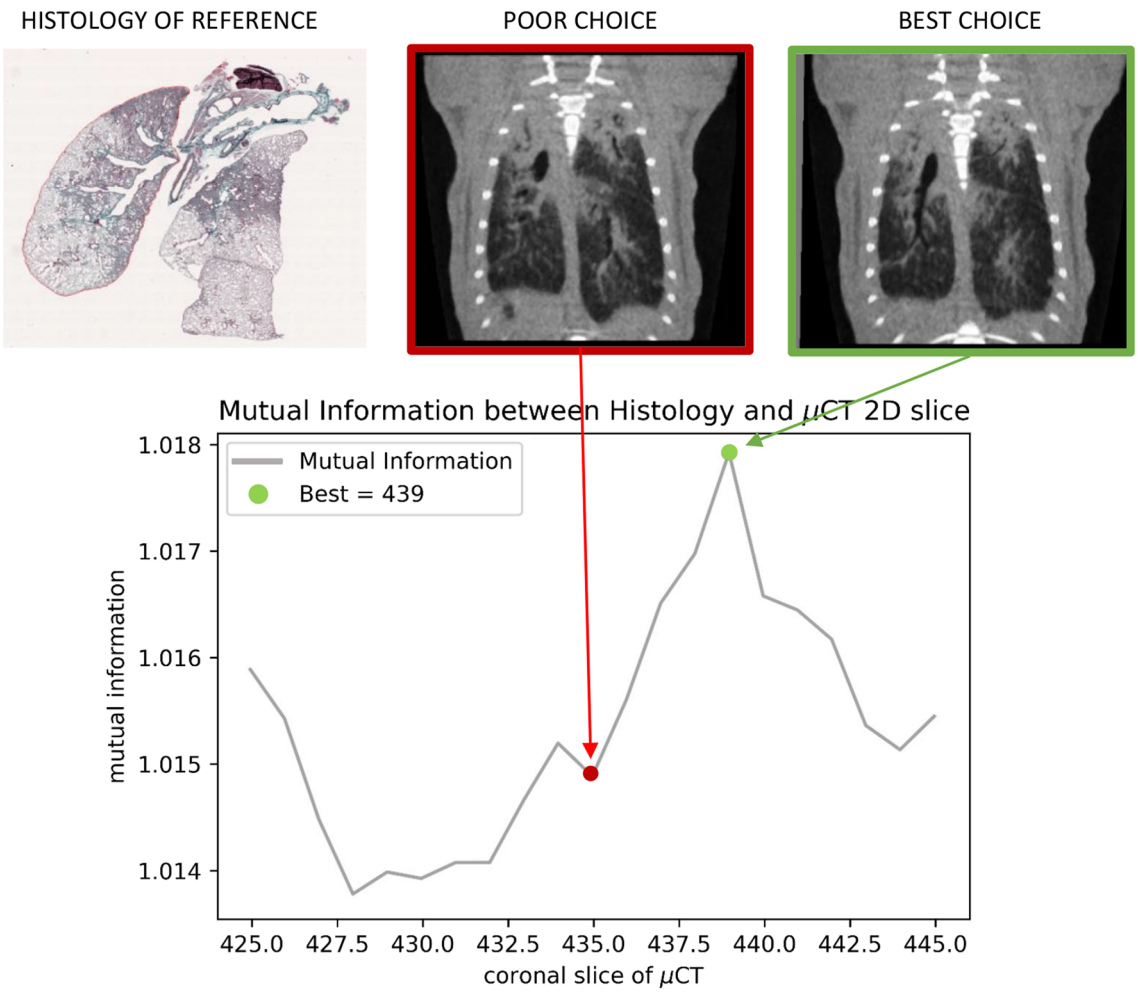

Fig. 4 Co-registration of the μCT with the histological section. Matching procedure. For each coronal micro-CT slice in the acceptability range, a mutual information value is calculated between the micro-CT slice and the histological slice. The slice with low mutual information (red dot) represents a poor choice, even though the structures of interest are present. The slice that maximizes the mutual information (green dot) is the best choice and is therefore selected by the algorithm

Table 1 Biomarkers derived from μCT coronal slices

Name	**Description**	**Units**	**Formula**
Area	Area of the left	mm^3	$voxelnumber \cdot voxelsize$
MLA	Mean lung attenuation	HU	$\sum_i^N \frac{HU_i}{N}$
Gas	Left lung area occupied by air	mm^3	$\frac{Area \cdot MLA}{(-1000HU)}$
Tissue	Left lung area without air	mm^3	$Area - Gas$
Ratio	Gas/tissue ratio	na	$\frac{Gas}{Tissue}$
Normo aerated area	Left lung area that is normo-aerated; reflects the number of no/mild lesions	mm^3	Voxels in range [– 630, – 307]
Hypo aerated area	Left lung area that is hypo-aerated; reflects the number of moderate lesions	mm^3	Voxels in range (– 307, – 45)
Non aerated area	Left lung area that is non-aerated; reflects the number of severe lesions	mm^3	Voxels in range [– 45, 230]
Hyper aerated area	Left lung area that is hyper-inflated; reflects regions with high gas/tissue ratio, due to e.g	mm^3	Voxels in range [– 830, – 630)

Results

Re-orientation

The accuracy of the re-orientation step was evaluated by comparing the rotation angles calculated manually with those inferred automatically. The overall Mean ± standard deviation (SD) of Absolute Error (MAE) on the x-axis was 2.7° ± 2.8° and 1.3° ± 1.2° on the z-axis. This included an outlier within the SAL cohort, which was due to an incorrect paraffin embedding of the specimen. The corrected MAE, calculated by excluding this outlier, is reported for the overall population and for each treatment group (SAL, BLM) in Table 2.

Slice selection

Figure 5 illustrates the difference between manually and automatically selected coronal slice numbers. We defined a match as 'perfect' when the manually selected slice was identical to the slice predicted by the tool (Fig. 5, black line). We deemed an error of up to 10 slices (equivalent to 0.5 mm) as 'acceptable', while larger discrepancies were flagged as 'glaring' errors. The matching tool demonstrated an overall success rate of 95%, which was calculated as the ratio between the sum of perfect and acceptable matches and the total number of matches:

$$Success\ rate = \frac{number\ of\ perfect + acceptable\ matches}{total\ number\ of\ matches}$$

In the SAL cohort, a perfect match was achieved in 5 out of 10 animals, corresponding to 50% of the entire group. For the remaining animals, the automatically selected slice differed from the manually selected one by fewer than 10 slices. In the BLM cohort, 27 out of 50 animals, i.e., 54% of the whole group, had a perfect match, while an acceptable match was obtained in 20 animals. Within the BLM group, the semi-automatic matching tool made significant errors in only 3 instances, corresponding to discrepancies of 17, 12, and 11 slices, or 0.85, 0.60, and 0.55 mm, respectively. Notably, the accuracy of the match was not affected by the location of the cutting plane within a ventral or a dorsal region of the lungs. These three cases of marked inconsistency were excluded from correlation analysis between CT-derived and histological parameters but were manually matched for further investigation.

Table 2 Absolute error between automatic and manual rotation angles in the re-orientation step (excluded the outlier)

Group	ΔX(°)	ΔZ(°)
BLM + SAL	2.2° ± 1.9°	1.3° ± 1.2°
BLM	1.7° ± 1.2°	1.2° ± 1.0°
SAL	3.0° ± 2.5°	1.6° ± 1.5°

Readout correlation

An example of a perfect match is shown in Fig. 6a, which highlights the accurate alignment of prominent pulmonary structures such as the main bronchi.

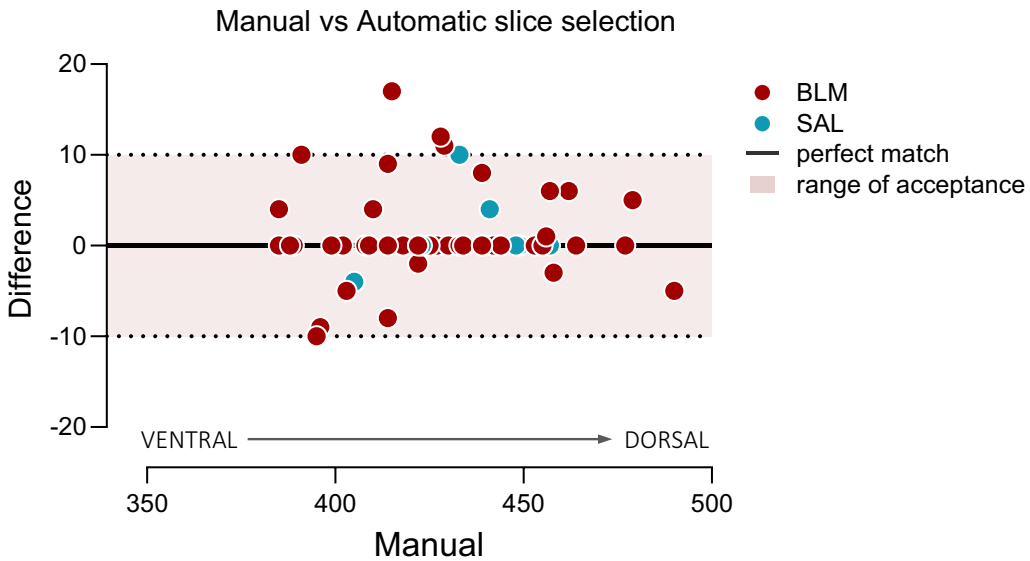

Fig. 5 Automatic vs Manual slice selection. Difference between automatic and manual selected slices vs manually selected slice number. A match was considered "perfect" when the manually selected µCT slice corresponded exactly with the one predicted by the tool (black line). Any error up to 10 slices, corresponding to 0.5 mm, was considered "acceptable" (shadowed area). Both fibrotic (BLM, red) and healthy (SAL, light blue) animals are included in the plots

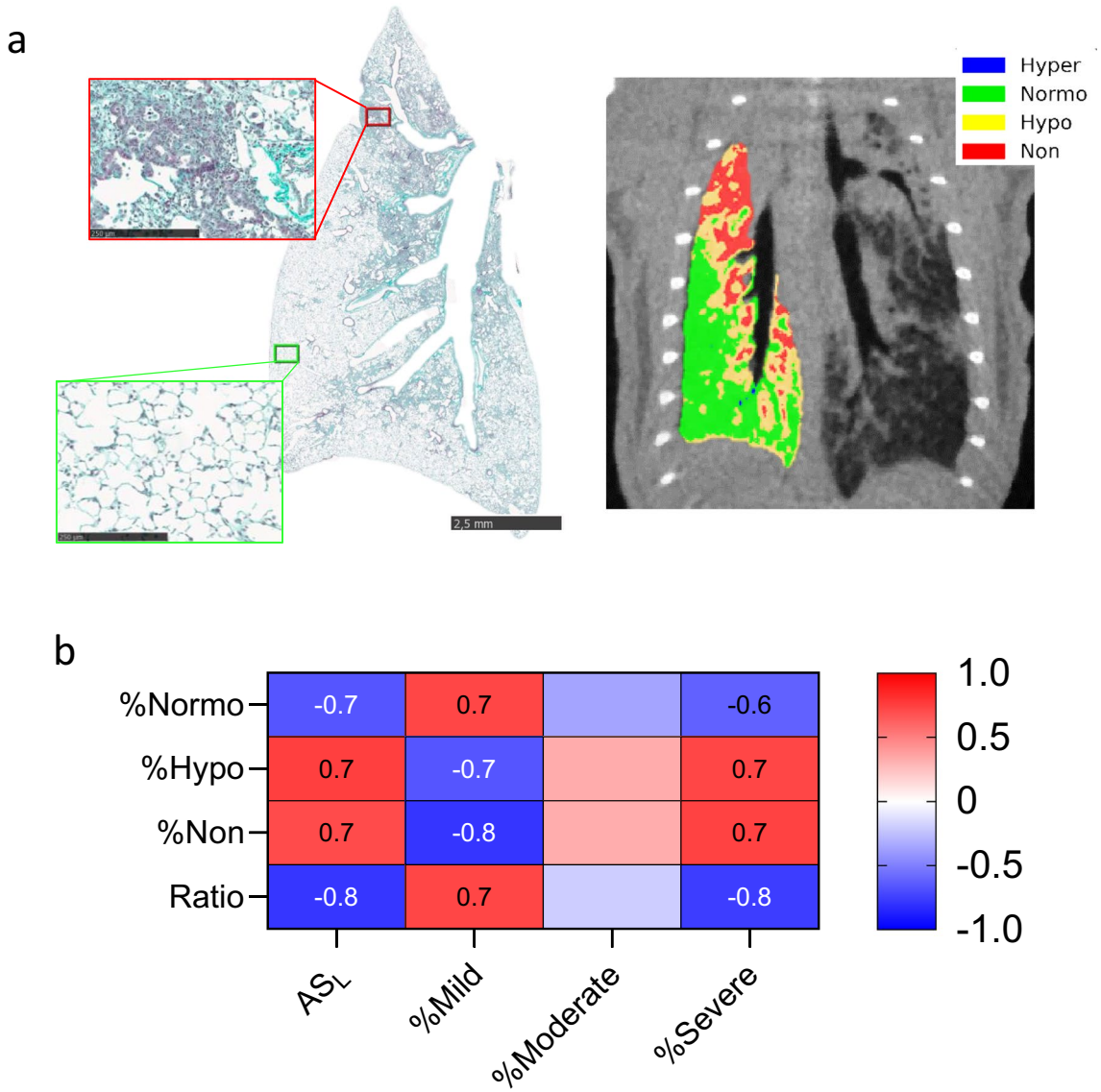

Fig. 6 Correlation of readouts. **a** Representative perfect match between a histological slice and the corresponding coronal µCT slice. On the left, the left-lobe histological slice, (bar corresponding to 2.5 mm). Regions of severe and mild fibrosis are magnified (bars corresponding to 250 µm) and respectively highlighted in red and green boxes. On the right, the corresponding 2D coronal µCT slice that automatically selected. The voxel of the left lung are classified into aeration compartments (Normo = green, Hypo = yellow, Non = red). **b** Heat-map representation of Spearman correlation coefficients (R) between µCT and histological-derived parameters derived in automatically matched slices. Non-significant ($p < 0.05$) correlations are not shown. The color bar indicates high positive correlations in red and high negative trends in blue

An excellent concordance between the most severe fibrotic lesions and non-aerated voxels as well as between mild or no fibrosis and normo-aerated areas became apparent upon examination of the morphological biomarkers and the aeration compartments derived from the µCT slice.

Spearman correlation analysis of 2D-densitometry and histological data (Fig. 6b) revealed a significant correlation ($p < 0.01$) between the left-lung Ashcroft score (AS_L) and all the CT-derived parameters expressed as percentages of the left lung area.

The correlation between CT-derived parameters and different grades of fibrosis (mild to severe) was confirmed upon subdivision of the AS_L values into different classes, with a slight improvement in the correlation between the %Non. However, no significant correlations were observed with the moderate fibrotic lesions.

Discussion

Despite significant progress in treating IPF, there remains an urgent need for novel, effective therapies capable of preventing or reversing lung fibrosis [2]. The development of innovative drugs relies not only on the accuracy of experimental animal models to replicate the disease but also on the effective evaluation of these models. In this pursuit, integrating various technologies to assess disease progression and treatment response at various stages of the trial becomes crucial [21]. µCT imaging has emerged as a powerful tool for in-vivo evaluation, providing dynamic insights into disease evolution and impact of therapeutic interventions by enabling individual monitoring of lung morphology, density, and function at different timepoints [6, 8, 21]. On the other hand, histological investigation provides a detailed microscopic assessment of lung tissue, complementing µCT imaging [29]. While µCT offers a non-invasive 3D view ideal for longitudinal studies, histology provides high-resolution, histo-morphometric data, but is invasive and needs expert interpretation. The co-registration of histological sections with corresponding 2D µCT scans can be considered a significant advance in preclinical research because it allows the extraction of functional and molecular biomarkers for the same subject, which can be used to accurately estimate disease severity or therapeutic intervention efficacy.

The method described here facilitates the identification of the µCT slice corresponding to a specific histological section, thus allowing for a robust synchronization of histological analysis and in vivo µCT data. As a result, the cross-talk between these two technologies is enhanced, reducing the time required for alignment from 40 min (manual) to just 5 min (automatic) and minimizing potential operator bias.

A key step of our procedure is the alignment of the µCT volume orientation with the configuration used during histological sample preparation. This is crucial for an accurate and reliable analysis, as any deviation or misalignment could introduce data inconsistencies and potential misinterpretations. Once the µCT volume is re-oriented, the proposed tool allows for sequential navigation through adjacent tissue slices, akin to a three-dimensional exploration of the sample. This unique feature of µCT underscores its complementarity with classical histological methodologies. While a histological section provides detailed information on a small fraction of the tissue thickness, the ability to navigate through the µCT volume offers a comprehensive, slice-by-slice view of the whole tissue. This multi-scale approach, which allows to transition from a histological section to the whole specimen, provides a deeper insight into the sample and uncovers structural information that might be missed by histology alone [12, 30]. Moreover, the use of µCT can guide the selection of the most representative region for histological examination, thus ensuring that histological data are indicative of the overall sample structure [31].

The precise inclusion of paired morphological details yielded by both imaging modalities is another fundamental prerequisite for accurate alignment. In this study, the left lung emerged as an ideal region of interest due to the maintenance of its structure post-paraffin embedding. Therefore, a step specifically dedicated to the segmentation of the left lung was implemented for both imaging modalities. For the µCT volume, segmentation is automated and relies on the DL method proposed by Vincenzi et al. [24], which was proved to be reliable across healthy and fibrotic tissue. On the other hand, the ROI on histology is defined by semi-automatic segmentation, facilitated by an application-specific intuitive interface. Although the development of highly refined segmentation methods was not the primary goal of our work, implementing a semi-automatic approach was crucial to reduce inter-subject variability in the segmentation of the histological dataset, proving robustness in delineating lung contours across varying degrees of fibrosis severity.

Co-registering multimodal and multiresolution images is a complex task. We addressed this issue by employing an affine registration framework designed to compensate for alterations induced by various factors such as tissue fixation, dehydration, and paraffin inclusion. The segmentation of the left lung guided the registration process, focusing on the lung boundary and dominant features such as the main airways. A key aspect of our approach is the use of normalized mutual information as a metric that quantifies the statistical relatedness between multimodal images, enabling effective alignments between different modalities, even with complex, non-linear intensity relationships. We chose normalized mutual information as a metric for its robustness in geometric transformations, flexibility with different imaging modalities, ability to capture complex relationships between pixels, and adaptability to the optimization algorithms used to guide the registration process [32].

Since no ground-truth exists for our matching framework, we conducted both qualitative and quantitative evaluations. The qualitative assessment demonstrated a high degree of accuracy (approximately 95%), considering key factors such as the presence of the main bronchi, and the shape of the left lung fibrotic lesions distribution. This spatial correspondence, which represents the most critical prerequisite for reliable analysis, facilitated the localization of structural changes in the lung and their correlation with histopathological features. Unlike previous studies [7, 9] that relied

on manual co-registration, our automated approach streamlines the overall process, with considerable time saving, enhanced workflow efficiency, and increased accuracy and reproducibility. For the quantitative evaluation of slice selection accuracy, we correlated µCT and histological parameters, as this represents the ultimate goal of the developed tool (i.e. establishing a precise linkage between quantitative CT-imaging and histological data). We observed significant correlations between all densitometric parameters derived from µCT analysis of the 2D coronal slice and the mean Ashcroft score of the left lungs. The "%Poorly" and the "Ratio" parameters achieved the highest R-squared values ($R^2 = 0.8$). Although the correlation between the two methodologies was very high, the exploration and possible inclusion of additional histological readouts such as collagen content [33, 34] or the ALI score [35] could provide further insight and potentially improve the interpretation of µCT data, thus enhancing our ability to distinguish between different types of structural impairment.

Although the present pipeline significantly improved the alignment of µCT and histological slices, it currently relies on a few manual steps. Future work will thus be aimed at increasing automation, in order to enhance the overall effectiveness of the process while minimizing user interactions. Prospective strategies in this direction may involve the automatic classification of mouse health status based on histology and the application of supervised AI models for histology-based lung segmentation, thereby providing valuable information on airway detection and further improving the processing pipeline as well as the accuracy of the method [36].

The proposed semi-automatic approach represents an initial but significant advancement toward a precise integration of ex-vivo cellular-level information with in-vivo morphological data for preclinical drug discovery in lung fibrosis. The three-dimensional visualization offered by µCT combined with detailed histological information allows for a more accurate and representative analysis of the tissue, providing a comprehensive structural context for the molecular data derived from histology. Consequently, the proposed approach improves the reliability and reproducibility of omic studies [37–39], representing the starting point for a multi-integrative platform in which transcriptomic and proteomic data from the same subject could be carefully combined to better understand the molecular process of fibrosis and aid in the discovery of new therapies By semi-automatically integrating these data types, we can gain a detailed and objective view of disease progression and response to treatment within a reasonable timeframe. While we tested the method only in healthy and BLM-treated mice, the pipeline is ready to be employed routinely in drug discovery trials to boost the assessment of drug efficacy for pulmonary fibrosis.

Moreover, the proposed pipeline can be readily adapted to other small animal models of respiratory diseases as well as to other imaging modalities such as MRI. It also sets the stage for different parallel applications, including CT "guided sectioning" for a more precise target acquisition during biopsies. As demonstrated by Albers et al. [12] and Stalder et al. [40], µCT data can aid the identification of the most representative histological slices, which typically represent less than 1% of the total lung volume [10], thus reducing the risk of biased conclusions resulting from limited sampling [29].

Furthermore, automated identification of the correct virtual histology slice from the 3D CT dataset not only will facilitate routine integration of these two examination modalities, but will also allow co-registration of previously matched slices, for example with the use of an elastic registration workflow such as the one proposed by Chicherova et al. [17].

Conclusions

In the present work, we described a semi-automatic process that effectively combines µCT parameters with collagen deposition measurements and other histological results in an animal model of pulmonary fibrosis. This system is instrumental to a detailed understanding of lung pathology and the development of a multi-layer integrative platform, potentially incorporating transcriptomics and proteomics data. A precise combination of informative, yet methodologically distinct datasets may aid the identification of novel therapeutic mechanisms, personalized treatment strategies, and innovative cures. Our integrated analytical platform can be applied to different animal models for drug discovery purposes and expanded to include other imaging modalities, paving the way to additional future applications such as CT-guided sectioning for more precise biopsy retrieval.

Abbreviations

µCT	Micro-computed tomography
AS	Ashcroft score
3D	Three-dimensional
2D	Two-dimensional
AS_L	Average Ashcroft score on the left lung
CNN	Convolutional neural network
DL	Deep learning
HU	Hounsfield unit
MAE	Mean absolute error
MLA	Mean lung attenuation
OA	Oropharyngeal aspiration
P01	End-inspiratory
P02	End-expiratory
ROI	Region of interest
SD	Standard deviation
VAS	Visual analogue scale
WSI	Whole slide images

Supplementary Information

The online version contains supplementary material available at https://doi.org/10.1186/s12967-024-05819-y.

Supplementary Material 1.

Acknowledgements
The authors thank Professor Simone Ottonello for the critical revision of the manuscript.

Author contributions
FFS, EV, MB, and EF conceived and designed the research. EV and AF participated in methodology and software development. EF performed in vivo experiments. MB analyzed data. MB, EF, DB, FP, FFS interpreted results. MB, EV, and FP prepared figures. FP, MB, EV, and FFS drafted the manuscript. EF, CB, AA, NS, and GV edited and revised the manuscript. All authors approved the final version of the manuscript.

Funding
This study was funded by Chiesi Farmaceutici, AdvaNced Technologies for Human-centrEd Medicine (ANTHEM), PNC0000003.

Availability of data and materials
The data sets used and/or analyzed during the current study are available from the corresponding author on reasonable request.

Declarations

Ethics approval and consent to participate
All animal experiments described herein were authorized by the official competent authority and approved by the intramural animal-welfare body (AWB) of Chiesi Farmaceutici and authorized by the Italian Ministry of Health (protocol number: 449/2016-PR). All procedures were conducted in compliance with the European Directive 2010/63 UE, Italian D.Lgs 26/2014, the revised "Guide for the Care and Use of Laboratory Animals" and with the 'Animal Research: Reporting of In Vivo Experiments' (ARRIVE) guidelines.

Consent for publication
Not applicable.

Competing interests
FFS, GV and EF are employees of Chiesi Farmaceutici S.p.A., which supported the research work. The remaining authors declare that the research was conducted in the absence of any commercial or financial relationships that could be construed as a potential competing interests.

Author details
[1]Camelot Biomedical Systems S.R.L, Genoa, Italy. [2]Department of Mathematical, Physical and Computer Sciences, University of Parma, Parma, Italy. [3]Molecular Imaging Facility, Experimental Pharmacology & Translational Science Department, Chiesi Farmaceutici S.P.A, 43122 Parma, Italy. [4]ANTHEM (AdvaNced Technologies for Human-centrEd Medicine), Spoke 3, Milan, Italy. [5]Department of Medicine and Surgery, University of Parma, Parma, Italy. [6]Dipartimento di Elettronica, Informazione e Bioingegneria, Politecnico di Milano, Milan, Italy.

Received: 27 August 2024 Accepted: 31 October 2024
Published online: 18 November 2024

References

1. Verleden SE, Tanabe N, McDonough JE, et al. Small airways pathology in idiopathic pulmonary fibrosis: a retrospective cohort study. Lancet Respir Med. 2020;8:573–84.
2. Raghu G, Rochwerg B, Zhang Y, et al. An official ATS/ERS/JRS/ALAT clinical practice guideline: treatment of idiopathic pulmonary fibrosis—an update of the 2011 clinical practice guideline. Am J Respir Crit Care Med. 2015;192:e3–19.
3. Hübner R-H, Gitter W, Eddine El Mokhtari N, et al. Standardized quantification of pulmonary fibrosis in histological samples. Biotechniques. 2008;44:507–17.
4. Tielemans B, Dekoster K, Verleden SE, et al. From mouse to man and back: closing the correlation gap between imaging and histopathology for lung diseases. Diagnostics. 2020;10:636.
5. Grandi A, Ferrini E, Zoboli M, et al. A mouse model of progressive lung fibrosis with cutaneous involvement induced by a combination of oropharyngeal and osmotic minipump bleomycin delivery. Am J Physiol-Lung Cell Mol Physiol. 2024;326:L736–53.
6. Buccardi M, Ferrini E, Pennati F, et al. A fully automated micro-CT deep learning approach for precision preclinical investigation of lung fibrosis progression and response to therapy. Respir Res. 2023;24:126.
7. Pennati F, Leo L, Ferrini E, et al. Micro-CT-derived ventilation biomarkers for the longitudinal assessment of pathology and response to therapy in a mouse model of lung fibrosis. Sci Rep. 2023;13:4462.
8. Khalajzeyqami Z, Grandi A, Ferrini E, et al. Pivotal role of micro-CT technology in setting up an optimized lung fibrosis mouse model for drug screening. PLoS ONE. 2022;17: e0270005.
9. Ruscitti F, Ravanetti F, Essers J, et al. Longitudinal assessment of bleomycin-induced lung fibrosis by Micro-CT correlates with histological evaluation in mice. Multidiscip Respir Med. 2017;12:8.
10. Mecozzi L, Mambrini M, Ruscitti F, et al. In-vivo lung fibrosis staging in a bleomycin-mouse model: a new micro-CT guided densitometric approach. Sci Rep. 2020;10:18735.
11. Ferrini E, Leo L, Corsi L, et al. A new anesthesia protocol enabling longitudinal lung-function measurements in neonatal rabbits by micro-CT. Am J Physiol-Lung Cell Mol Physiol. 2021;321:L1206–14.
12. Albers J, Markus MA, Alves F, et al. X-ray based virtual histology allows guided sectioning of heavy ion stained murine lungs for histological analysis. Sci Rep. 2018;8:7712.
13. Becker K, Stauber M, Schwarz F, et al. Automated 3D–2D registration of X-ray microcomputed tomography with histological sections for dental implants in bone using chamfer matching and simulated annealing. Comput Med Imaging Gr. 2015;44:62–8.
14. Lundin EL, Stauber M, Papageorgiou P, et al. Automatic registration of 2D histological sections to 3D microCT volumes: trabecular bone. Bone. 2017;105:173–83.
15. Sarve H, Lindblad J, Borgefors G, et al. Extracting 3D information on bone remodeling in the proximity of titanium implants in SRμCT image volumes. Comput Methods Programs Biomed. 2011;102:25–34.
16. Chicherova N, Fundana K, Müller B, et al. Histology to μCT data matching using landmarks and a density biased RANSAC. Berlin: Springer; 2014. p. 243–50.
17. Chicherova N, Hieber SE, Khimchenko A, et al. Automatic deformable registration of histological slides to μCT volume data. J Microsc. 2018;271:49–61.
18. Khimchenko A, Deyhle H, Schulz G, et al. Extending two-dimensional histology into the third dimension through conventional micro computed tomography. Neuroimage. 2016;139:26–36.
19. Museyko O, Marshall RP, Lu J, et al. Registration of 2D histological sections with 3D micro-CT datasets from small animal vertebrae and tibiae. Comput Methods Biomech Biomed Eng. 2015;18:1658–73.
20. National Research Council. Guide for the care and use of laboratory animals. Washington, D.C.: National Academies Press; 2011. https://doi.org/10.17226/12910.
21. Buccardi M, Grandi A, Ferrini E, et al. Micro-CT-assisted identification of the optimal time-window for antifibrotic treatment in a bleomycin mouse model of long-lasting pulmonary fibrosis. Sci Rep. 2024;14:14792.
22. Barbayianni I, Ninou I, Tzouvelekis A, et al. Bleomycin revisited: a direct comparison of the intratracheal micro-spraying and the oropharyngeal aspiration routes of bleomycin administration in mice. Front Med. 2018. https://doi.org/10.3389/fmed.2018.00269.
23. Mambrini M, Mecozzi L, Ferrini E, et al. The importance of routine quality control for reproducible pulmonary measurements by in vivo micro-CT. Sci Rep. 2022;12:9695.
24. Vincenzi E, Fantazzini A, Basso C, et al. A fully automated deep learning pipeline for micro-CT-imaging-based densitometry of lung fibrosis murine models. Respir Res. 2022;23:308.

25. Grandi A, Ferrini E, Mecozzi L, et al. Indocyanine-enhanced mouse model of bleomycin-induced lung fibrosis with hallmarks of progressive emphysema. Am J Physiol-Lung Cell Mol Physiol. 2023;324:L211–27.
26. Rother C, Kolmogorov V, Blake A. GrabCut. ACM Trans Graph. 2004;23:309–14.
27. Jonic S, Thevenaz P, Unser MA. Multiresolution-based registration of a volume to a set of its projections. Bellingham: Spie; 2003. p. 1049.
28. Mattes D, Haynor DR, Vesselle H, et al. Nonrigid multimodality image registration. Bellingham: Spie; 2001. p. 1609–20.
29. Jenkins RG, Moore BB, Chambers RC, et al. An official American Thoracic Society workshop report: use of animal models for the preclinical assessment of potential therapies for pulmonary fibrosis. Am J Respir Cell Mol Biol. 2017;56:667–79.
30. Yuan R, Nagao T, Paré PD, et al. Quantification of lung surface area using computed tomography. Respir Res. 2010;11:153.
31. Varma M, Collins LC, Chetty R, et al. Macroscopic examination of pathology specimens: a critical reappraisal. J Clin Pathol. 2024;77:164–8.
32. Pluim JPW, Maintz JBA, Viergever MA. Mutual-information-based registration of medical images: a survey. IEEE Trans Med Imaging. 2003;22:986–1004.
33. Wegner KA, Keikhosravi A, Eliceiri KW, et al. Fluorescence of picrosirius red multiplexed with immunohistochemistry for the quantitative assessment of collagen in tissue sections. J Histochem Cytochem. 2017;65:479–90.
34. Courtoy GE, Leclercq I, Froidure A, et al. Digital image analysis of picrosirius red staining: a robust method for multi-organ fibrosis quantification and characterization. Biomolecules. 2020;10:1585.
35. Lindstedt S, Wang Q, Niroomand A, et al. High resolution fluorescence imaging of the alveolar scaffold as a novel tool to assess lung injury. Sci Rep. 2024;14:6662.
36. Viswanathan VS, Toro P, Corredor G, et al. The state of the art for artificial intelligence in lung digital pathology. J Pathol. 2022;257:413–29.
37. Ricard-Blum S, Miele AE. Omic approaches to decipher the molecular mechanisms of fibrosis, and design new anti-fibrotic strategies. Semin Cell Dev Biol. 2020;101:161–9.
38. Bo C, Zhang J, Sai L, et al. Integrative transcriptomic and proteomic analysis reveals mechanisms of silica-induced pulmonary fibrosis in rats. BMC Pulm Med. 2022;22:13.
39. Li D, Liu Y, Wang B. Identification of transcriptomic markers for developing idiopathic pulmonary fibrosis: an integrative analysis of gene expression profiles. Int J Clin Exp Pathol. 2020;13:1698–706.
40. Stalder AK, Ilgenstein B, Chicherova N, et al. Combined use of micro computed tomography and histology to evaluate the regenerative capacity of bone grafting materials. Int J Mater Res. 2014;105:679–91.

Publisher's Note